Phys Chem Minerals (2014) 41:709–723
DOI 10.1007/s00269-014-0685-x

ORIGINAL PAPER

Numerical models of ionic diffusion in one and three dimensions: application to dehydration of mantle olivine

Catherine Thoraval · Sylvie Demouchy

Received: 19 December 2013 / Accepted: 12 May 2014 / Published online: 31 May 2014

Abstract The hydrogen content of nominally anhydrous minerals is of great interest, because it can influence many physical and mechanical properties of mantle rocks. Moreover, the hydrogen diffusion profiles can be used to constrain timescales related to magma eruptions. Here, we report models of ionic diffusion for trace elements in anisotropic crystals and apply them to hydrogen diffusing out of mantle-derived olivine. We first compare and discuss the characteristics of 1D and 3D models and show that only 3D anisotropic diffusion models can lead to diffusion profiles exhibiting non-equilibrium plateau at the center of the solid along the slowest axis, as measured in natural samples. In a second part, we discuss the differences between hydration and dehydration of olivine for diffusion that is linked to two different atomic sites involved in hydrogen mobility. Finally, we apply our 3D anisotropic model to previous results on mantle-derived olivine from Pali-aike to better characterize diffusion coefficients and their anisotropy that could be relevant for dehydration of olivine. Our results show that dehydration has to be strongly anisotropic, with a fast [100] axis and a significantly slower [001] axis.

Keywords Ionic diffusion · Mineral · Olivine · Hydrogen · Dehydration · Numerical model · Finite difference · Three dimensions

Electronic supplementary material The online version of this article (doi:10.1007/s00269-014-0685-x) contains supplementary material, which is available to authorized users.

C. Thoraval (✉) · S. Demouchy
CNRS, UMR 5342 Geosciences Montpellier, Université Montpellier 2, 34095 Montpellier, France
e-mail: catherine.thoraval@gm.univ-montp2.fr

Introduction

Extensive mantle degassing during early Earth's accretion is considered to have led to massive to total hydrogen loss (Albarède 2009; O'Neill 1991). However, the Earth's mantle rocks still contain a significant amount of water in various forms of speciation (H_2O, H_2 OH^-), as shown by the water amount found in volcanic glasses, MORB and OIB (few wt%, e.g., Dixon and Clague 2001, H_2 in glasses was reported in Gaillard et al. 2003 and H_2O and OH^- in glasses in Ihinger et al. 1994 as well as in nominally anhydrous minerals (NAMs) from mantle-derived peridotites (e.g., Ingrin and Skogby 2000; Bolfan-Casanova 2005; Bercovici and Karato 2003; Hirschmann et al. 2005). Several studies (Ingrin and Skogby 2000; Bolfan-Casanova 2005; Marty 2012) have suggested that the Earth's mantle may contain up to 3–11 times the ocean mass (i.e., of the order of 10^{22} kg), making the Earth's mantle a potential major reservoir in the Earth's water cycle. Moreover, the question of the deep mantle water cycle is of key interest since rocks' properties such as electrical conductivity (Karato 1990; Yoshino et al. 2009), seismic properties (Jacobsen et al. 2004), phase stability (Wood 1995), melting temperature (Gaetani and Grove 1998) and viscosity (Mackwell et al. 1985; Mei and Kohlstedt 2000; Demouchy et al. 2012) are sensitive to small amount of water (i.e., at the level of few wt ppm H_2O). Hence, many mantle processes such as convection or differentiation may strongly depend on the mantle's water content, its speciation, transport by diffusion and partitioning (during melting or metasomatism) in the Earth's upper mantle.

As mentioned before, water can be found as molecular water and hydroxyl group in silicate melts and glasses (Ihinger et al. 1994; McMillan 1994), structurally in hydrous minerals (Deer et al. 1997) and also as atomic

hydrogen impurities incorporated as point defects within the crystalline structure in NAMs (e.g., Beran and Putnis 1983; Ingrin and Skogby 2000). Olivine is particularly important for the water's cycle since it is the most abundant phase in the Earth's upper mantle (60–80 % in volume). Previous studies have assessed that hydration and then dehydration of olivine are governed by ionic diffusion, which controls chemical exchanges toward different crystalline solids and fluid phases (Mackwell and Kohlstedt 1990; Kohlstedt and Mackwell 1998).

In olivine, hydrogen may occupy three different atomic sites: (1) a metallic (Me) site in the octahedron, (e.g., Mg^{2+}), and/or (2) a silicon site, replacing partially Si^{4+} in tetrahedron, and/or (3) in an interstitial site (e.g., Beran and Putnis 1983; Nakamura and Schmalzried 1983; Mackwell and Kohlstedt 1990; Kohlstedt et al. 1996; Padrón-Navarta et al. 2014). Results from experiments on solubility of hydrogen in olivine (e.g., Kohlstedt et al. 1996; Férot and Bolfan-Casanova 2012) have strongly favored the hypothesis that hydrogen dominantly occupies metal vacancies in olivine. Hydrogen could also occupy Si vacancy as simple defect (Brodholt and Refson 2000; Ingrin et al. 2013) or as associated defects with Ti (Berry et al. 2007a, b). However, concentration of Si defects is likely to be significantly less abundant than concentration of Me vacancies since in the Earth's mantle, olivine is almost always coexisting with pyroxenes (i.e., thus, the activity of silica is buffered in the system and Si vacancies in olivine are very unlikely to occur in significant concentration). Moreover, at moderate high pressure (<1 GPa), the proportion of interstitial hydrogen is likely to be a function of the presence and amount of Fe^{3+} in the olivine structure (Mackwell and Kohlstedt 1990; Zhao et al. 2004).

Experimental studies of the kinetics of hydrogen incorporation (hydration) in olivine single crystals have identified the coexistence of two different processes for diffusion, involving two different types of atomic sites (Mackwell and Kohlstedt 1990; Kohlstedt and Mackwell 1998). First, protons (hydrogen), which sit in interstitial sites, diffuse, and this flux is counter balanced by a polaron flux (a polaron can be described as a electron hole in the crystalline structure). This process is assumed to be dependent on Fe^{2+}/Fe^{3+} ratio in olivine. We will refer to it as the proton–polaron process (PP). Second, protons sit in Me vacancies, which are usually occupied by Mg or Fe in natural iron-bearing olivine, we will refer to it as the proton–vacancy process (PV). Based on hydration experiments at low-confining pressure (300 MPa), it was shown that at low temperature (<1000 °C) or short time (1 h), PP process is the fastest mechanism and the first mechanism to start H diffusion, it will then dominate the incorporation rate at this time or temperature range. To the contrary, at higher temperature (>1000 °C) or for long-run duration (>3 h), PV, which is a slower mechanism than PP, will complete incorporation until equilibrium concentration is reached (Mackwell and Kohlstedt 1990; Kohlstedt and Mackwell 1998; Demouchy and Mackwell 2003, 2006). Results of solubility experiments (Kohlstedt et al. 1996) have shown as well that reaching equilibrium (solubility) involves mainly the occupancy of metallic sites by H and that little hydrogen is stored as interstitials. Recent Fourier transform infrared (FTIR) spectroscopy measurements at low temperature (from −194 to 200 °C) has questioned the main site for H storage (Ingrin et al. 2013), but without clear conclusion for consequences at temperature relevant of the upper mantle where FTIR absorption spectra of OH^- in olivine seems to be different (Yang and Keppler 2011). In addition, both PP and PV processes appear to be highly anisotropic in olivine with the fastest direction of diffusion parallel to [100] axis for the PP process, but parallel to [001] axis for the PV process (Mackwell and Kohlstedt 1990; Kohlstedt and Mackwell 1998; Demouchy and Mackwell 2003, 2006). Experimental studies have provided sets of diffusion equations, one for each crystallographic axis and for each mechanism of H diffusion in olivine (Demouchy and Mackwell 2006) as well as for PV in forsterite (Demouchy and Mackwell 2003). These studies are based on FTIR analysis which allow to address the anisotropy of ionic diffusion, when at contrary step-heating, commonly used in the noble gaz community, can only constrain bulk diffusion and is hence inappropriate for assessing the anisotropy of hydrogen diffusion in olivine. For hydration, the two processes having different anisotropy were so far treated separately (Kohlstedt and Mackwell 1998). However, this might not be accurate for dehydration when more than one type of point defects are coexisting all along the diffusion progression.

Our knowledge on diffusion mechanism of hydrogen in olivine is essentially derived from a few experimental studies and is not currently supported by ab initio modeling of atomic transport despite progress on diffusion modelization for crystalline structure (e.g., Walker et al. 2003; Karki and Verma 2009).

The concentration of hydrogen in olivine crystals is mostly measured using FTIR spectroscopy. It takes the form of concentration profiles across a doubly polished crystal grain, parallel to one of the principal crystallographic axis or as close as possible to one of them (Peslier and Luhr 2006; Demouchy and Mackwell 2003; Denis et al. 2013). Hydrogen concentration profiles have been recorded for a very few natural mantle-derived olivines, and the FTIR analyses remain challenging (Peslier and Luhr 2006; Demouchy et al. 2006; Denis et al. 2013) due to samples' size, irregular or damaged grain's shapes and alteration by hydrous minerals. Magma times of residence or magma ascent rates have been estimated from such

concentration profiles (H or Fe–Mg) measured on natural samples from the analytical solution for diffusion in one dimension (1D) where the ionic diffusion coefficients are those obtained experimentally. (e.g., Costa and Dungan 2005; Demouchy et al. 2006; Costa et al. 2008). Recently, a user-friendly Matlab-based program for 1D multi-element diffusion in olivine has been proposed by Girona and Costa (2013). However, these approaches are not suitable to describe strongly anisotropic diffusion, such as hydrogen diffusion in olivine.

Here, we have developed models of ionic diffusion in crystals for various geometries (Fig. 1): plane sheet diffusion in 1D, radial isotropic diffusion in a sphere (3D radial), isotropic and anisotropic diffusion in a 3D prism. We compare the results of 3D and 1D modeling and test the limitation of a 1D approach relative to 3D. We perform numerical experiments with our 3D anisotropic model when the diffusing species is strongly anisotropic (i.e., more than one order of magnitude between the diffusion coefficients along the fastest and slowest crystallographic axes). Both PP and PV processes are tested individually or combined, and we discuss the differences between hydration and dehydration.

Finally, we attempt to use the new 3D anisotropic models to explain and fit the data from the mantle-derived olivine from Pali-aike (mantle xenoliths in alkali basalt from southernmost Patagonia) reported previously by Demouchy et al. (2006).

Model

Equations for diffusion

Diffusion of atomic species in a solid, a liquid or a gas is a transport phenomenon which leads to an equalization of the concentration without requiring bulk motion. Here, we focus on the ionic diffusion in a crystalline solid.

We consider first the simple case in one-dimensional geometry (i.e., in dimension x) as illustrated in Fig. 1a and commonly referred as 1D diffusion in a plane sheet (Crank 1975, chapter 4, see also Costa et al. 2008).

The Fick's first law relates the flux J_x of particles to the gradient $\partial C/\partial x$ of concentration of the species i (not noted) and the diffusion coefficient D according to:

$$J_x = -D\frac{\partial C}{\partial x} \tag{1}$$

The negative sign shows that the diffusive flux goes from the higher concentrations toward the smaller concentrations.

The Fick's second law expresses the conservation law for the diffusive species:

$$\frac{\partial C}{\partial t} = -\frac{\partial J_x}{\partial x} = D\frac{\partial^2 C}{\partial x^2} \tag{2}$$

The first term (i.e., the time partial derivative) corresponds to the accumulation (or loss) rate, while the second (the space partial derivative) represents the balance between the input and output diffusive fluxes, expressed in the third term according to Eq. 1.

The generalization of the Fick's laws from 1D to 3D requires using vector notation. For an isotropic media, the Fick's first law is written as:

$$\bar{J} = -D\nabla C \tag{3}$$

The diffusion flux $\bar{J}$ is a vector, which direction is opposite to the concentration gradient vector ∇C (∇ being the differential operator for gradient) as for the 1D case. D is the diffusion coefficient and C is the concentration of the diffusive species.

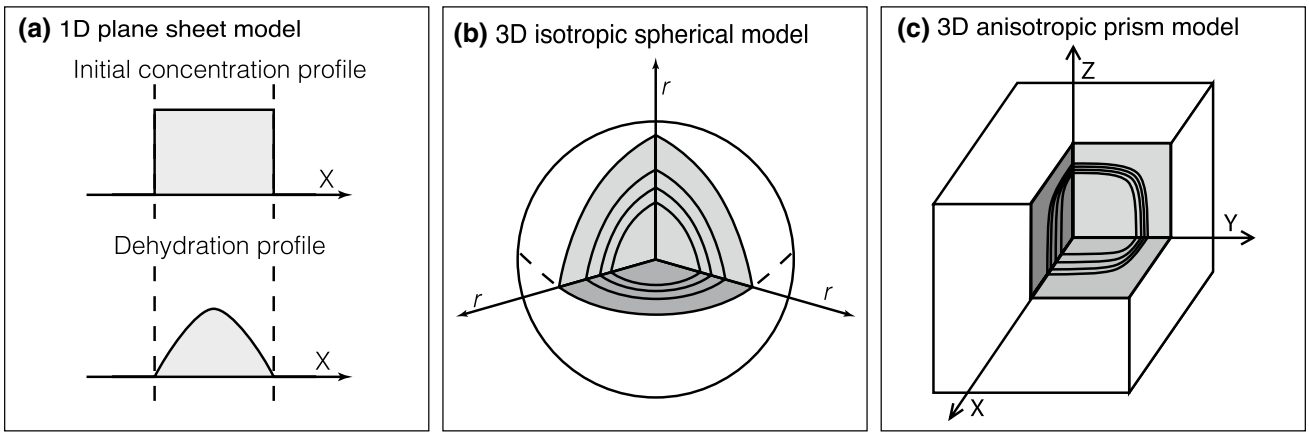

Fig. 1 Sketches of the diffusion schemes used for **a** 1D, **b** 3D isotropic spherical and **c** 3D prism models. Diffusion is illustrated by concentration profiles in 1D case and by iso-concentration contours in 3D cases

In a 3D anisotropic media, the diffusion properties depend on the direction and are characterized by a second rank diffusion tensor $\bar{\bar{D}}$. Fick's first law is written:

$$\bar{J} = -\bar{\bar{D}}\nabla C \tag{4}$$

In an orthorhombic crystal-like olivine, the principal axes of diffusion coincide with the axes of crystallographic symmetry (Mehrer 2007 p. 33). Writing Eq. 4 in Cartesian coordinates along these axes (where x, y and z stand for [100], [010], [001] crystallographic axis, respectively) shows how the anisotropy affects the diffusion vector, which is no more parallel to the gradient vector:

$$\begin{aligned} J_x &= -D_x \frac{\partial C}{\partial x} \\ J_y &= -D_y \frac{\partial C}{\partial y} \\ J_z &= -D_z \frac{\partial C}{\partial z} \end{aligned} \tag{5}$$

D_x, D_y and D_z are the diffusion coefficients along the principal crystallographic axes [100], [010] and [001], respectively.

One can retrieve the isotropic case from Eq. 5 by taking the same diffusion coefficients in all directions, $D = D_x = D_y = D_z$.

The Fick's second law for diffusion relates the variation of concentration with time to the variation of concentration with space, as detailed in the 1D case above. Under the assumption that the diffusion coefficients are not varying in the media considered; thus, the diffusion coefficient is not function of the concentration in "i"; the Fick's second law can be expressed in Cartesian coordinates as:

$$\frac{\partial C}{\partial t} = D_x \frac{\partial^2 C}{\partial x^2} + D_y \frac{\partial^2 C}{\partial y^2} + D_z \frac{\partial^2 C}{\partial z^2} \tag{6}$$

which simplifies as follows for an isotropic media:

$$\frac{\partial C}{\partial t} = D\left(\frac{\partial^2 C}{\partial x^2} + \frac{\partial^2 C}{\partial y^2} + \frac{\partial^2 C}{\partial z^2}\right) \tag{7}$$

Numerical models

We have developed models based on finite differences for solving the Fick's second law for diffusion in 1D plane sheet (Fig. 1a), in 3D radial (see details below, and Fig. 1b) and in 3D Cartesian geometry for isotropic and anisotropic 3D prism (Fig. 1c). We assume that the diffusion coefficients are neither space nor concentration dependent, since the concentrations of hydrogen in the considered mineral (olivine or forsterite) are very low (i.e., trace element at ppm level).

The derivatives are expressed as central differences, and the set of equations is solved using an Euler's explicit scheme: the concentrations at grid points at each time step are expressed as a function of the previous time step. This scheme allows us to account for a variation of diffusion coefficients with time, hence accounting for potential temperature dependence with time. Thanks to the symmetry properties of olivine (orthorhombic, space group Pbnm), the system can be solved for only one half in 1D and one-eighth in 3D, see Fig. 1c. The choice of the grid is made to ensure the accuracy of the solution. The time step is chosen as a function of the space step in order to insure the stability of the solution. The numerical parameters are the grid spacing and the time step. The numerical models have an asymptotic behavior when refining the grid.

At initial conditions, the sample is homogeneous with a constant concentration of the species considered everywhere in the solid. At the beginning of the numerical experiment (time $t = 0$), the concentration at the sides (i.e., surface of the solid) is set to zero.

We have developed a model for diffusion in an isotropic sphere (call 3D radial) since it is a similar calculation as the 1D plane sheet model. Indeed, considering radial isotropic diffusion illustrated in Fig. 1b, the Fick's second law for diffusion in an isotropic media (Eq. 3) expressed in spherical coordinates is reduced to its radial dependence according to:

$$\frac{\partial C}{\partial t} = D\left(\frac{\partial^2 C}{\partial r^2} + \frac{2}{r}\frac{\partial C}{\partial r}\right) \tag{8}$$

where r is the radius varying from 0 (center of the sphere) to R (radius of the spherical sample). Rewriting Eq. 8 using the new variable $u = r\,C$ leads to

$$\frac{\partial u}{\partial t} = D\frac{\partial^2 u}{\partial r^2} \tag{9}$$

Equation 9 is similar to the 1D Cartesian equation (Eq. 2) and can be solved the same way in order to determine the values of u for each value of r. The concentration can then be calculated according to $C = u/r$. The value of concentration at the center ($r = 0$) cannot be strictly calculated and is set to the same value as the closest grid point.

The models are used in this study to investigate the effect of the geometry and dimension on the anisotropic diffusion of hydrogen in an anisotropic crystalline solid such as olivine. They could also be used for solid diffusion of other elements such as minor and trace elements in olivine or in other anisotropic crystals.

As mentioned before, the choice of an explicit scheme to solve the differential equations allows us to be able to account for variation of diffusion coefficients with time, by adjusting their values at each time step.

The numerical codes have been written in Fortran 77, and the results of the 1D model have been successfully compared with the analytical solutions for the 1D case.

Parameterization

We describe here the physical parameters, since the choice of the numerical parameters (grid spacing and time step) has been discussed above. The physical parameters are the characteristics of the sample (size and diffusion properties) and the description of the conditions of the numerical experiment (temperature, initial concentration and boundary conditions).

Two sets of parameters have been used. The first one has been chosen so that the results of the different models can be easily compared between each other. The second set of parameters is chosen so that the results of numerical experiments can be compared to natural specimens. In both cases, the diffusion coefficients for H are taken from Kohlstedt and Mackwell (1998) and Demouchy and Mackwell (2006), respectively, for the PP and the PV processes. The relationship to chemical diffusion simplified $\tilde{D} \approx D_i$, i the diffusing species, [see Kohlstedt and Mackwell (1998) for details]; however, complex dependence can be implemented as well.

For the calculation sets presented in the result section, the sample is 3 mm long in the 1D plane sheet models; the diameter of the sample is 3 mm for the 3D radial models; and in the 3D prism models (both isotropic and anisotropic case), the size of the sample is 3 × 3 × 3 mm. The temperature is fixed to 1000 °C. The values for the corresponding diffusion coefficients are given in Table 1 and already illustrate the anisotropy.

The initial concentration is homogeneous in the samples and set to 50 ppm wt H_2O, which is a realistic value for hydrogen concentration in garnet-bearing peridotites (based on water content quantification following the calibration of Paterson; Paterson 1982; see also Bell and Rossman 1992; Demouchy et al. 2006).

Combination of the two diffusion mechanisms

The PP process is significantly faster than the PV process: The diffusion coefficient along the fast [100] axis for the PP process is about 40 times faster at 1000 °C than the diffusion coefficient along the fast [001] axis for the PV process (see Table 1). Diffusion according to PP process involves interstitial sites, corresponding to a small concentration of H (noted C^*, see Fig. 2), as opposed to PV process, which involves vacant sites with higher concentrations and hence allowing maximum equilibrium concentration (noted S as for solubility) (Fig. 2). Since the respective diffusivities of each mechanism are so different, they may appear as successive and independent during hydration, while they could be hypothetically interactive during dehydration (Fig. 2).

We have considered here combination of the two mechanisms for dehydration by allocating the initial hydrogen concentration at equilibrium partly to interstitial sites, which will dehydrate following PP process, and partly to vacancy sites, which will dehydrate following PV process. The two diffusion systems are solved separately (i.e., not a true interaction, see Fig. 2). The total concentration is simply the sum of the two concentrations, both decreasing from initial concentrations. Interstitial and vacancies (the later assumed to be mostly metallic vacancies) are hence considered as separated reservoirs of protons with independent behaviors (Fig. 2).

Results

Diffusion in 1D and 3D, single process

Here, we present the results of each model and point out their differences. The 1D plane sheet, 3D radial models, as well as the 3D isotropic case have been computed for the three same diffusion coefficients (corresponding to the principal diffusion axes, Table 1) and for each process (PP or PV) in order to be comparable with the results of the fully 3D anisotropic case. The characteristics of each model will be evaluated by comparisons of the variation of concentration at the center of the solid with time for the different cases as shown in Fig. 3. The description of the concentration profiles across the solid (hereafter called diffusion profiles) when the concentration at the center has reached half the initial value (i.e., 25 ppm wt H_2O) as depicted in Fig. 4, for the three crystallographic axes [100], [010] and [001], for two diffusive mechanisms and the four

Table 1 Diffusion coefficients of hydrogen in olivine crystal at 1000 and 1245 °C for both PP and PV processes

	Diffusion coefficient along each axis (m^2/s)		
	[100]	[010]	[001]
1000 °C			
PP (Kohlstedt and Mackwell 1998)	1.57×10^{-10}	6.17×10^{-12}	4.29×10^{-12}
PV (Demouchy and Mackwell 2006)	1.32×10^{-13}	1.32×10^{-13}	1.01×10^{-12}
1245 °C			
PP (Kohlstedt and Mackwell 1998)	1.43×10^{-9}	9.60×10^{-11}	2.30×10^{-11}
PV (Demouchy and Mackwell 2006)	2.96×10^{-12}	2.96×10^{-12}	5.17×10^{-11}

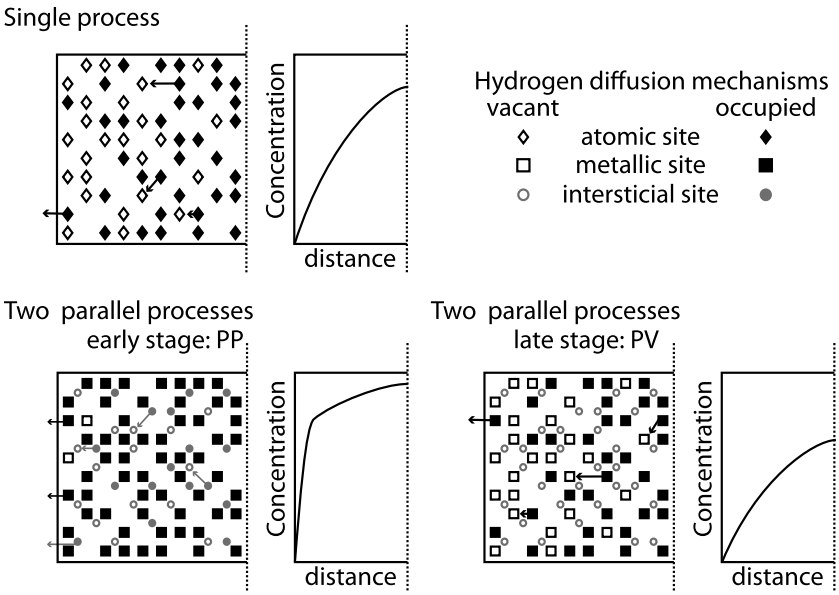

Fig. 2 Illustration of the hydrogen diffusion mechanisms in an olivine crystalline lattice for **a** diffusion in (based on Kohlstedt and Mackwell 1998; Demouchy and Mackwell 2006) and for **b** diffusion out (this study). Only sites occupied or which could be occupied by hydrogen are shown (as a hypothetic array) and not the entire lattice with all atomic sites or point defects. See text for details. *Abbreviation S* = solubility, achievable only with the second process (proton–vacancy), *C** = maximum concentration achieved with the first process (proton–polaron)

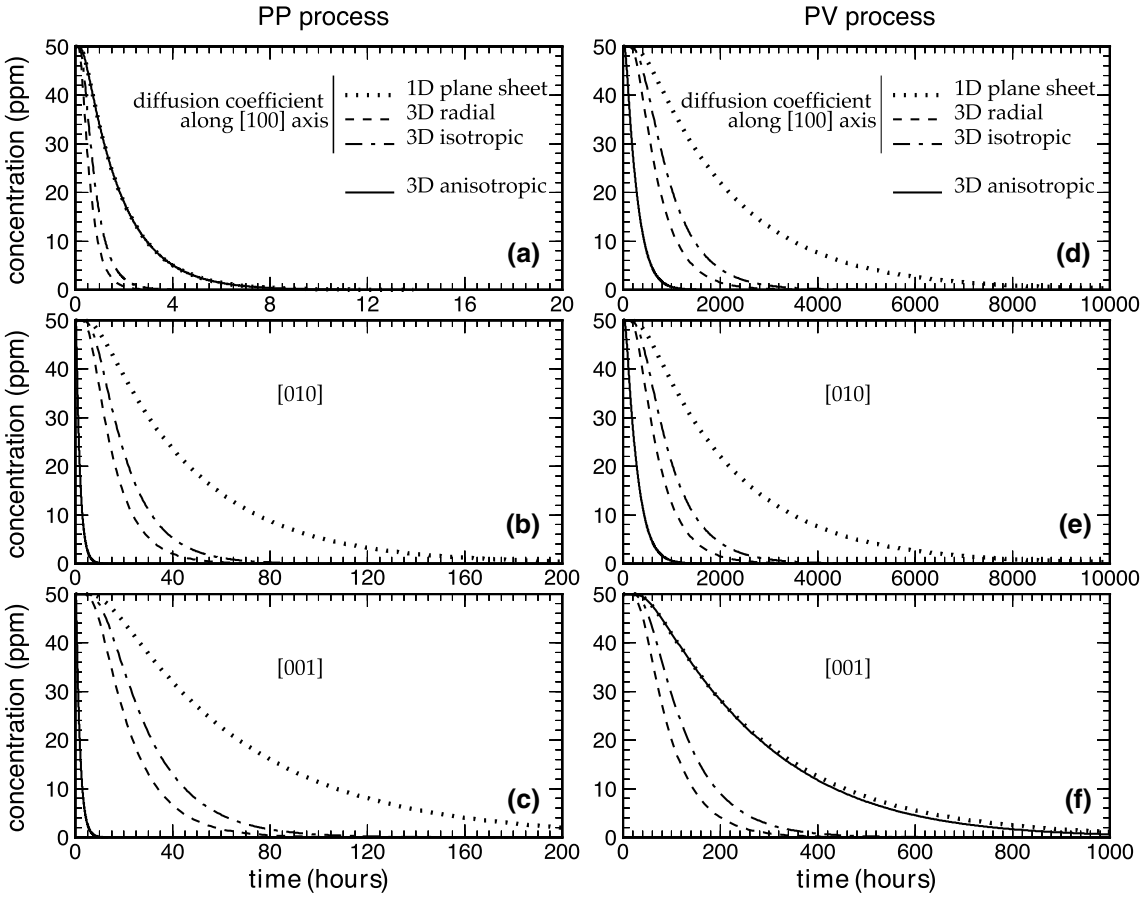

Fig. 3 Modeled decrease of hydrogen concentration at the center of the olivine crystal as a function of dehydration duration. The diffusion coefficients are from Kohlstedt and Mackwell (1998) for the PP process and from Demouchy and Mackwell (2006) for the PV process. Diffusion is modeled for a constant temperature of 1000 °C. Models are for a sample of 3 mm in length of 1D plane sheet diffusion (*dotted line*), a sample of 3 mm in diameter for 3D radial diffusion (*dashed line*), a sample of 3 × 3 × 3 mm in size for 3D isotropic diffusion in a prism (*dotted-dashed line*) and a sample of 3 × 3 × 3 mm in size for 3D anisotropic diffusion in a prism (*solid line*). Initial concentration is 50 ppm wt H_2O

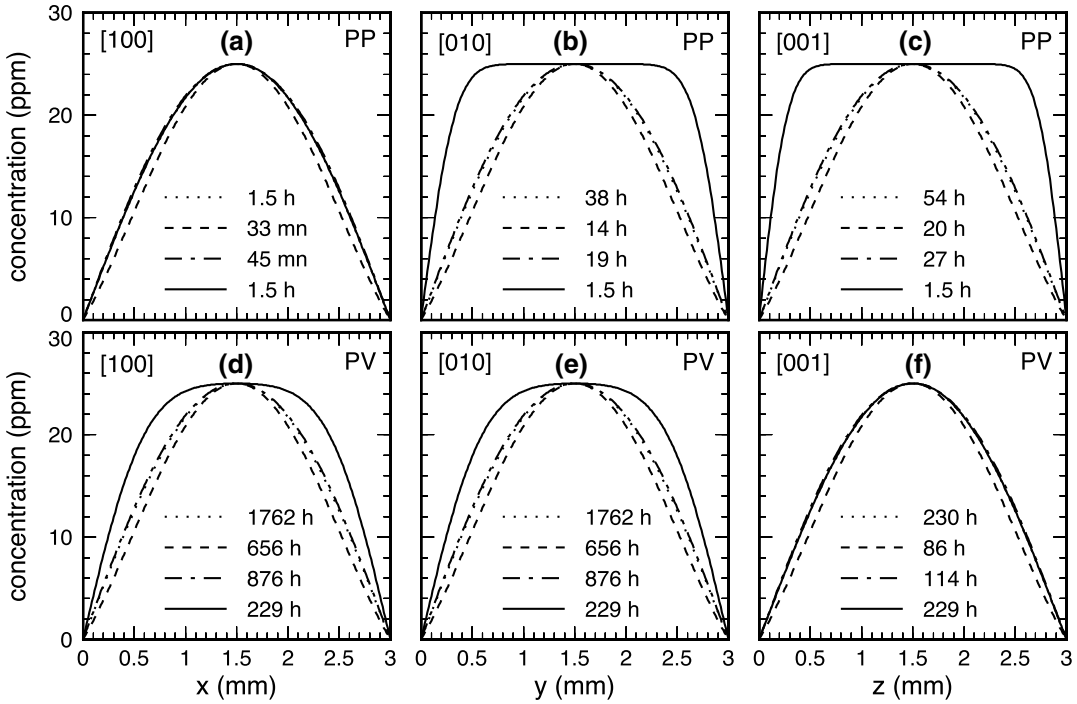

Fig. 4 Hydrogen concentration profiles along the three crystallographic axes of an olivine crystal during diffusion out for both PP and PV processes. Diffusion is modeled for a temperature of 1000 °C. Models are for a sample of 3 mm in length of 1D plane sheet diffusion (*dotted line*), a sample of 3 mm in diameter for 3D radial diffusion (*dashed line*), a sample of 3 × 3 × 3 mm in size for 3D isotropic diffusion in a prism (*dotted-dashed line*) and a sample of 3 × 3 × 3 mm in size for 3D anisotropic diffusion in a prim (*solid line*). Initial concentration is 50 ppm wt H_2O. The profiles are shown for the concentration at the center equals half of the initial value (i.e., 25 ppm wt H_2O). Duration needed to reach this value is indicated for each case

models; 1D plane sheet (dotted line), 3D radial (dashed line), 3D isotropic (dotted-dashed line) and 3D anisotropic (solid line).

In all cases, dehydration starts from the rim to the center of the solid. During this first stage, the concentration at the center stays at its initial value; it ends when the concentration at the center of the sample starts to decrease and asymptotically tends to zero. The calculations have been stopped when the concentration at the center of the sample reaches 0.01 ppm wt H_2O, which is far below the 1 ppm wt H_2O detection limit using the FTIR analysis. This slowing down of dehydration process is due to the fact that diffusion flux decreases when the concentration gradient decreases, and hence, in the case of dehydration, when the concentration at the center of the sample decreases. The first diffusion stage, that is before the concentration at the center starts to decrease, occurs in all cases and appears clearly in Fig. 3f as a plateau for about 40 h in all diffusion models. In other cases, the duration of the early stage may vary depending on the model, the axes and the process. However, it does not exceed 5 % of the total dehydration duration in all cases.

The timescales used in Fig. 3 are chosen from the duration of total dehydration estimated for the 1D models since it is always the slowest, as shown as dotted curves in Fig. 3. For the 1D plane sheet dehydration according to PP process, the duration of total dehydration is of the order of 8 h for the fast [100] axis, of order of 200 h for the [010] axis and of the order of 300 h for the [001] axis. For the 1D plane sheet dehydration according PV process, the duration of total dehydration is of the order of 1000 h (~42 days) for the fast [001] axis and of 10000 h (1.1 year) for the slow axes ([100] and [010]), as a result of the diffusion coefficient along the [001] axis being eight times higher than along the [100] and [010] axes.

The 3D anisotropic model shows the same decrease of concentration at the center of the sample with time as the 1D model for the fastest axis as shown in Fig. 3a and f where the solid line is used for the 3D anisotropic model. This can be understood as the diffusion vector being parallel to the fastest axis. However, this is measurable only if the difference between the fastest and slowest diffusivity directions is important (i.e., >factor of 5). The discrepancy between the dotted line (1D plane sheet model) and the solid line (3D anisotropic model) observed for PV process in Fig. 3f after about 250 h (10.5 days) illustrates the fact that diffusion along the slowest axes cannot always be neglected.

In all cases, the 3D radial (dashed lines) and the 3D isotropic models (dotted-dashed lines) show behaviors close to each other, both faster than the 1D plane sheet models. Dehydration of the 3D radial (dashed lines) is always slightly faster than the 3D isotropic prism model. The time needed to reach half the initial concentration at the center of the sample is about 75 % shorter for the 3D radial model when compared to the 3D isotropic prism model, as noted in Fig. 4. This is due to the difference of geometry between the two solids. The 3-mm-diameter sphere (3D radial) is inscribed in a 3-mm-edge cube and thus having a volume about 48 % smaller than the volume of the cube. In other words, the diffusion profiles illustrated in Fig. 4 for 3D isotropic or anisotropic cases are calculated for the shortest path throughout the 3-mm-edge cube, which corresponds to the sphere diameter. The differences in the geometries are further illustrated in Fig. S1, which also depicts the concentration profiles across the sphere and along the shortest and longest (diagonal) paths across the cube in which the sphere in inscribed. The profile along the diagonal joining two opposite vertices is 1.7 times longer in distance than a direction parallel to an edge.

The diffusion profiles with the concentration at the center of the solid equal to the half of its initial value are shown for the different cases in Fig. 4, and the duration needed to reach this concentration value is indicated for each case. The shape of the diffusion profiles is the same for the 1D, 3D radial, 3D isotropic prism and 3D anisotropic prism along the fastest axes ([100] for PP and [001] for PV) with the maximum concentration value is at the center, and the concentration decreasing toward the rim. The form of the curve is indicating the concentration gradient along the corresponding axis. The diffusion profiles within the 3D radial model are slightly narrower than for the 1D cases and the 3D isotropic cases (however, within the analytical error bar for hydrogen measurements by FTIR), thus illustrating a steeper concentration gradient across the sample. The diffusion profiles for the anisotropic cases show different profiles along the different crystallographic axes. The diffusion profiles along the fastest axis ([100] for the PP process and [001] for the PV process) in 3D anisotropic cases are hardly distinguishable from the diffusion profiles along the same axis in the 1D and 3D isotropic prism models (i.e., Fig. 4a for PP, Fig. 4f for PV), as opposed to the diffusion profiles along the slowest axes shown as solid lines in Fig. 4b–e which are characterized by a plateau at the center of the solid with a constant concentration value. The diffusion profiles along the slowest axes consequently exhibit steep concentration gradients at the rim. An important outcome for the 3D anisotropic prism model is that the concentration of the plateau at the center of the solid is not the initial concentration, but the maximum concentration of the diffusion profile along the fastest axis.

Comparison of the results for the 1D plane sheet model and the 3D anisotropic model (Figs. 3, 4) demonstrates that the 1D model is a good approximation for diffusion along the fastest axis of diffusion in a 3D anisotropic solid, both for the duration and the shape of the diffusion profile. However, only the 3D anisotropic prism model outlines a concentration plateau in diffusion profiles along the slowest axes at all stages of dehydration. In 3D, the value of the concentration at the center of the sample, which is also the value of the concentration plateau, is governed by the fast axis. The 1D model cannot produce the diffusion profiles specific to the slowest axis observed in the profiles from the 3D anisotropic model of diffusion.

In our numerical experiments, the 3D radial model and the 3D isotropic prism models display similar concentration profiles and durations. However, the differences between the diffusion profiles illustrate that the geometry of the sample (here, sphere versus prism) may play a significant role in diffusion and may have implications for the determination of diffusion coefficients or dehydration durations from concentration profiles.

The differences between the models can be further assessed by comparing the concentration profiles obtained with the PV mechanism, after the same duration of dehydration (250 h) as shown in Fig. 5. The concentration profiles for the slow [100] and [010] axes in Fig. 5a, b are characteristic of the first stage of dehydration for 1D, 3D isotropic prism and spherical cases, where the concentration at the center of the solid is indeed close to the initial value of 50 ppm wt H_2O. The profiles from the 1D sheet and the 3D isotropic prism models cannot be distinguished at this stage, even if the decrease of concentration with time is faster for the 3D model than for the 1D model, as shown in Fig. 3d, e. On the contrary, the diffusion profiles along the fast [001] axis show that the concentration at the center of the solid has already decreased down to a value of 23 ppm wt H_2O for both the 1D and the 3D anisotropic prism models in Fig. 5c, and to less than 5 ppm wt H_2O for both the 3D radial and the 3D prism isotropic cases. After 250 h, the diffusion profiles in Fig. 5 show that the concentration at the center of the solid is only about 2 ppm wt H_2O less for the 3D radial case (dashed lines) than for the 3D prism isotropic case (dotted-dashed lines). The diffusion profiles for the 3D prism anisotropic case again show a plateau at the center of the sample along the slowest axes. The value of the concentration for these plateaus corresponds to the maximum concentration value at the center of the solid for the profile along the fastest [001] axis. We cannot find a duration allowing us to illustrate the same profiles for the PP mechanism, because for this process, the diffusion along the [001] axis is more than 25 times faster than along the two other axes. Thus, the total dehydration duration for cases involving the fast axis [100] is lower than the time

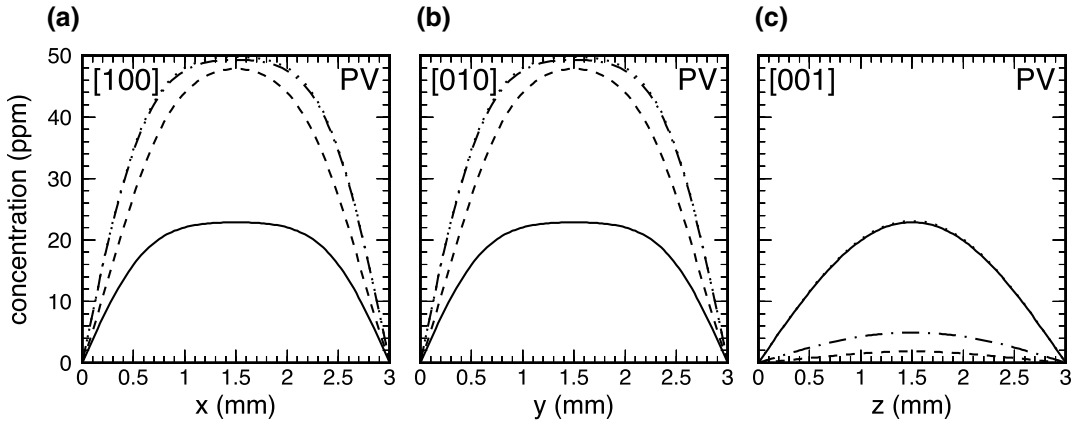

Fig. 5 Hydrogen concentration profiles showing the 3D effect within an anisotropic prism for the three crystallographic axes of an olivine crystal during diffusion out by PV process only, after 250 h, at 1000 °C. Models are for a sample of 3 mm in length of 1D plane sheet diffusion (*dotted line*), a sample of 3 mm in diameter for 1D spherical diffusion (*dashed line*), a sample of 3 × 3 × 3 mm in size for 3D isotropic diffusion in a prism (*dotted-dashed line*) and a sample of 3 × 3 × 3 mm in size for 3D anisotropic diffusion in a prim (*solid line*). Initial concentration is 50 ppm wt H_2O

needed for the other directions to significantly evolve from the initial conditions with constant concentration throughout the entire solid.

Diffusion in 3D, combination of two anisotropic processes

We show the results of a numerical experiment for dehydration as the two PP and PV processes acting on a priori defined separated reservoirs not interacting with each other and with a different concentration of potential sites occupied by H. We have computed the dehydration concentration profiles across a prismatic solid along the three principal axes of olivine. The concentrations of 10 and 40 ppm wt H_2O were chosen a priori to represents the concentrations initially allocated to the PP process and the PV process, respectively. The resulting profiles, in Fig. 6a, are drawn for concentration at the center of the solid from 49 down to 1 ppm wt H_2O, and with 2 ppm steps. The decrease of the concentration at the center of the solid with time is shown in the Fig. 6b. A zoom at the early stage of dehydration is shown in Fig. 6c, corresponding to the very rapid dehydration occurring by PP process. It takes about 10 h to release the entire 10 ppm wt H_2O reservoir dedicated to PP process at 1000 °C. The diffusion profiles from the subsequent PV process are shown in Fig. 6a for each axis as solid lines below the dashed lines, which represent the 40 ppm wt H_2O concentration initially allocated to PV process. The shapes of the diffusion profiles above 40 ppm wt H_20 at the center of the sample are characteristic of the dehydration according to PP process as described earlier, with almost parabolic profiles for fast [100] direction and plateau profiles for the slower directions [010] and [001]. The differences between the 41 ppm wt H_2O profile (above the dashed line) and 39 ppm wt H_2O profile (below the dashed line) illustrate the fact that the dehydration evolves from the PP process to the PV process. It is worth noticing that this evolution takes 44 h. The concentration at the center of the sample remains constant (40 ppm wt H_2O) for about 30 more hours corresponding to the first stage of dehydration (Fig. 6a) as described earlier for a single process (Fig. 3). From 39 ppm wt H_2O at the center of the solid and below, the concentration profiles are characteristic of the PV process as described earlier, with a plateau at the maximum concentration which corresponds to the concentration at the center of the sample along [100] and [010] slow axes and an almost parabolic profile along fast [001] direction. It takes about 900 h (37.5 days) to dehydrate the whole sample at 1000 °C (Fig. 6b). It needs to be mentioned that any other a priori choice of the concentrations, respectively, dedicated to the PP and the PV processes would not change the behavior described in this section characterized by a very rapid dehydration of the PP reservoir, whatever its size, followed by a much slower decrease of the remaining amount of hydrogen according to PV process.

Discussion

Diffusion mechanisms and concentration profiles

The results described in previous section show that the 1D plane sheet models are a good approximation for dehydration along the fastest axis of diffusion, assuming that the anisotropy is strong enough, that is, with diffusion coefficient along the fastest axis at least 5–10 times the diffusion coefficients along the other (slower) axes. In this case, the

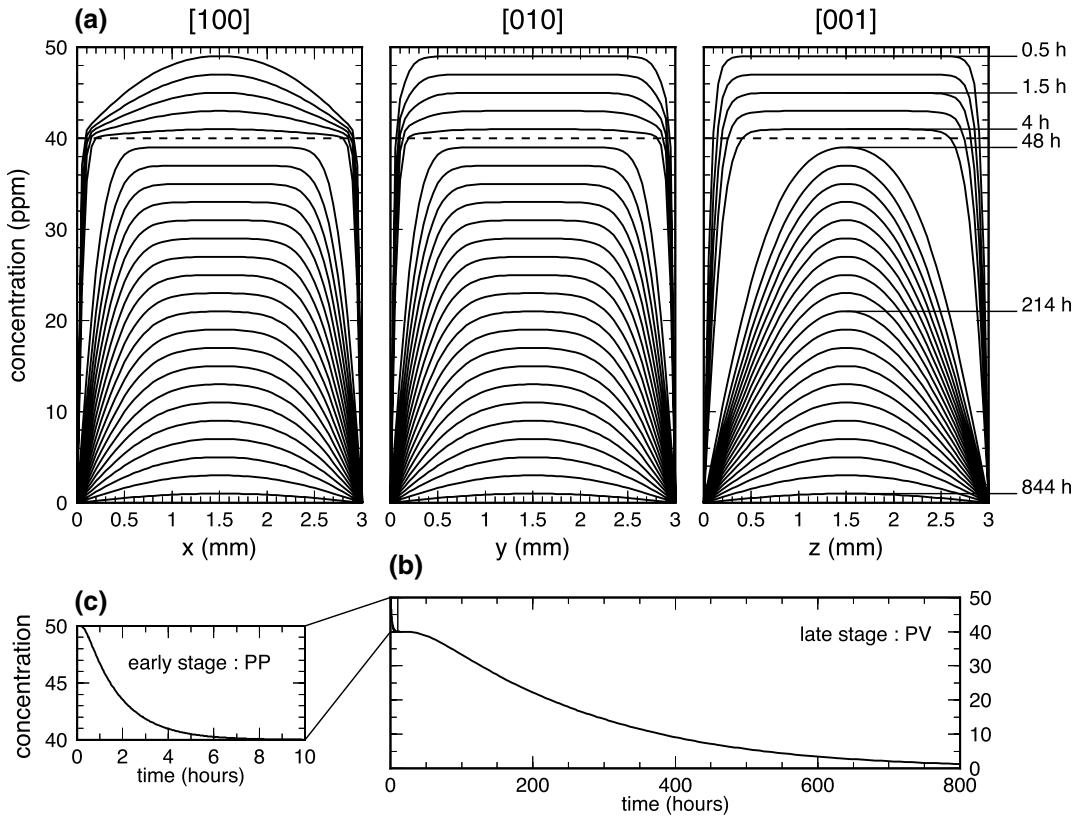

Fig. 6 **a** Modeled hydrogen concentration profiles for dehydration in 3D (anisotropic) along the three crystallographic axes of an olivine crystal with juxtaposed PP and PV processes (see text). Total initial concentration of hydrogen is 50 with 10 ppm wt H_2O allocated to interstitial sites (dehydration according to PP process) and 40 ppm wt H_2O allocated to metallic sites (dehydration according to PV process). The diffusion coefficients for PP and PV processes at 1000 °C are taken from Kohlstedt and Mackwell (1998) and from Demouchy and Mackwell (2006), respectively. **b** Decrease of the concentration at the center of the prismatic crystal with time, with a zoom in from (3b) in (3c) showing the very early stage corresponding to the very rapid dehydration due to the PP process

1D model is accurate to describe both the decrease of the concentration at the center of the solid with time and the concentration profile along the fastest axis. The 1D models can depict plateaus as well, but only in the first stage, when diffusion has not yet reached the center of the sample. In the 1D models, the value of the concentration at the plateau corresponds to the initial concentration. As soon as the concentration at the center of the solid starts to decrease, 1D model cannot yield a concentration profile with a concentration plateau. The decrease of the concentration at the center of the sample in 3D anisotropic diffusion is governed by the fastest diffusion coefficient and only 3D anisotropic models permit to obtain a concentration plateau along the slower axes, which is not corresponding to the initial concentration. To use the values from a short concentration plateau as a proxy of the initial hydrogen concentration (i.e., in the mantle source) can thus be very misleading.

Our results show that an accurate description of the geometry of the sample is important since the results of isotropic diffusion in a sphere (3D radial) and in a 3D prism are slightly different. However, the 3D radial model is a coarse, but satisfying approximation for a 3D isotropic prism, within a few percent for similar size and duration.

The attempt to model dehydration as combination of the PP and the PV processes, as it appears to occur for hydration, results in exhibiting PP-specific profiles at early stages (short duration) and PV-specific profiles at late stages. Considering the two processes separately is relevant for hydration, since the PP process is much faster than PV, then PP and PV can be considered as happening successively and then also independently. Indeed, after the early stage, there are no more interstitial sites available, and hence, there are no more PP fluxes. The interstitial and the metallic sites can hence be considered as separated reservoirs for incorporating hydrogen. However, this might not be relevant for dehydration since the interstitial sites are becoming available as protons move outwards as illustrated in Fig. 2. We can foresee that the protons may move from metallic sites to interstitial sites and vice versa so that the path of a proton exiting the crystal may be complex. Accounting for such interactions between the two processes at an atomic level may be responsible for diffusion coefficients specific

to dehydration. Properly describing such type of diffusion interactions at atomic level would require numerical constrains, which are not currently at hand, such as accurate concentrations of each point defects incorporating H as a function of pressure and temperature; and more importantly, the energies for site exchange for H in iron-bearing olivine, as well as their temperature dependency (activation energy).

Application to natural specimens

The peridotitic olivine from Pali-aike alkali basalt from Patagonia analyzed by Demouchy et al. (2006) depicts diffusion profiles along [100] and [001] axes, which have been compared to modeled profiles for the PV process only. Indeed, dehydration according to the PP process, because it is very rapid, would result in completely flat profiles (i.e., final concentration equals 0) for realistic magma ascent rates. Moreover, since the assumed initial concentration 312 ppm wt H_2O significantly exceeds the measured concentration of hydrogen of 46 ppm wt H_2O, the only mechanism capable of transporting approximatively 260 ppm wt H_2O out of the sample seemed to be the PV process (PP is considered to be limited to less 5 ppm wt H_2O). Thus, it was the mechanism considered as active in Demouchy et al. (2006) and Denis et al. (2013).

The measured concentration profiles from Pali-aike (Demouchy et al. 2006) exhibit the characteristics of a fast [100] axis (almost parabolic shape) and a slower [001] axis (plateau shape), mismatching the behavior of dehydration according to the PV process, but in agreement with recent results on hydrogen distribution around hydrous melt inclusion by Le Voyer et al. (2014). Here, we hence propose to empirically adjust the diffusion coefficients under the assumption that both mechanisms interact at atomic level as discussed in the previous section.

For the application to the Pali-aike olivine, the size of the sample used in 3D anisotropic model is 2.3 × 1.7 × 1.6 mm, slightly modified from Demouchy et al. (2006) so that the measured diffusion profiles respect symmetry, ensuring that the concentration maximum is located at the center of the sample. This is necessary to satisfy the assumption that the diffusion coefficients are constant in the whole sample. The initial concentration is fixed to 312 ppm wt H_20 (following the calibration from Bell et al. 2003) deduced from the water content in pyroxene (see Demouchy et al. 2006 for details). We assume that at depth, any major or trace elements are at equilibrium and that the initial H concentration profile is flat at this initial value.

We use the 3D prism anisotropic model described in the previous sections (Fig. 7). At first, we assume that the temperature and hence the diffusion coefficients are constant during dehydration since basalt magma ascent is considered to be adiabatic and almost isothermal (Giberti and Wilson 1990; Kavanagh and Sparks 2009; effect of temperature gradient is treated later in this section). For a given set of diffusion coefficients, the calculation is stopped when the concentration at the center of the sample reaches 46 ppm wt H_20, as in the natural specimen. The concentration profiles are then compared to the observations, and the corresponding dehydration duration is noted. The diffusion coefficients (D_x, D_y and D_z for the [100], [010] and [001] axes, respectively) used as reference (starting point) are those given for the PV process at 1245 °C by Demouchy and Mackwell (2006). We use a forward-modeling approach and define the diffusion coefficient sets for which there is a satisfying match to the measured profiles. Since concentration profiles have been measured only along [100] and [001] axes, it cannot be expected to perfectly constrain relative values of diffusion coefficients along the three directions of the olivine crystal.

The duration of dehydration from 312 to 46 ppm wt H_2O according to PV process at the constant temperature of 1245 °C is 2.9 h. The corresponding concentration profiles are drawn as grey lines in Fig. 7. We can see that the plateau of calculated diffusion profile along [100] axis in Fig. 7a is not in agreement with the measurements. The modified diffusion coefficients along [100], [010] and [001] will be hereafter denoted D_x', D_y' and D_z', respectively. In a first step, diffusion coefficient along [100] axis is increased ($D_x' = 10\ D_x$) to account for an hypothetic mobility of hydrogen from metallic sites to interstitial sites, hence favoring diffusion according to the PP process while the diffusion coefficients along [010] and [001] axes remain unchanged ($D_y' = D_y$ and $D_z' = D_z$). The corresponding concentration profiles are shown as black solid lines in Fig. 7a. The concentration profiles along [100] and [001] axes both show maximum concentration at the center with no plateau, since D_x' and D_z' are of the same order of magnitude ($D_x'/D_z' = 0.57$). The only plateau is observed along [010] axis, which is now the slowest axis, D_y' being about 20 times smaller than the fastest direction of diffusion. The concentration profile along [100] provides a satisfying fit to the measurements; however, the [001] axis seems to be too fast to best fit the data (Fig. 7a).

In a second numerical experiment, D_x and Dy are increased in the same way ($D_x' = 10\ D_x$ and $D_y' = 10\ D_y$), assuming that they behave the same way, as it is the case for PV process. D_z is reduced until it fits the measured profiles. The concentration profiles are shown in Fig. 7b for four values for D_z'. The four concentration profiles along [100] and [010] are hardly distinguishable from each other. The change in shape for the concentration profile along [001] axis appears to be very sensitive to the value of D_z'. A good fit for concentration profiles along [100] and [001]

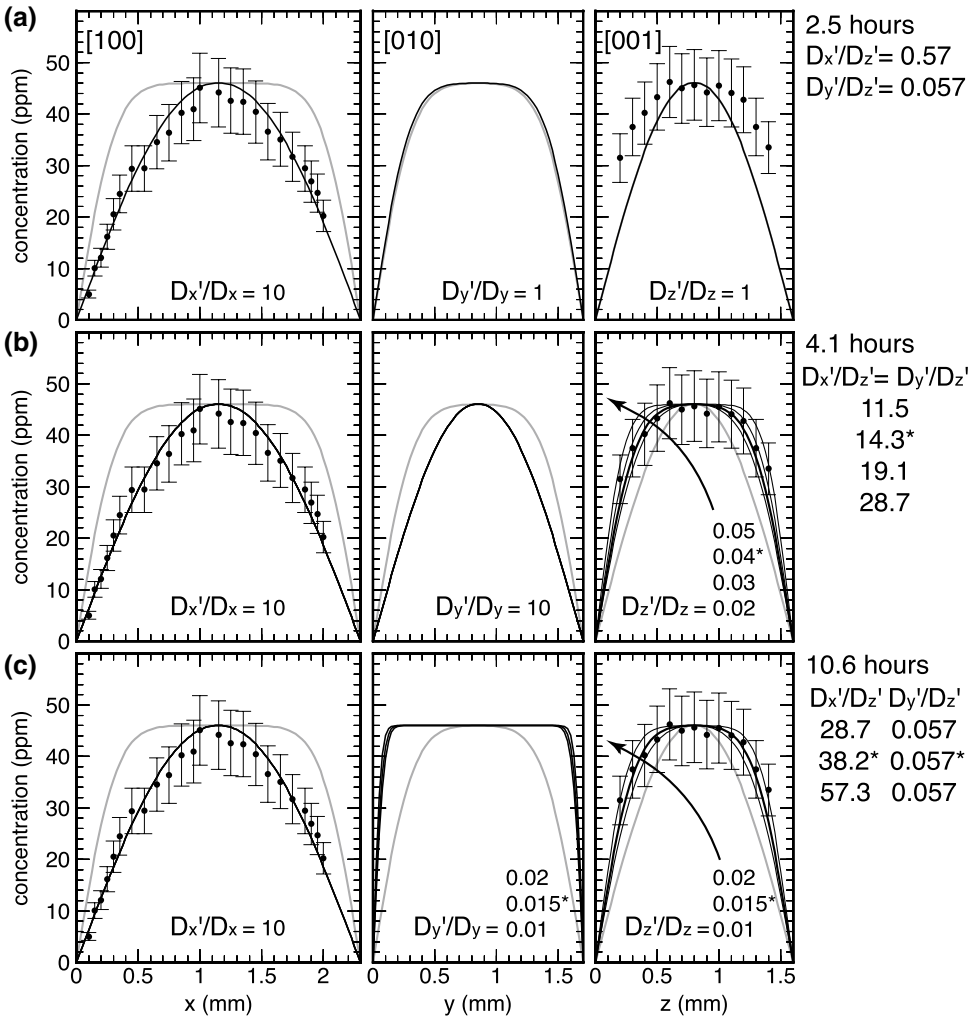

Fig. 7 Comparisons between the measured hydrogen concentration profiles for the PA-7 olivine from Pali-aike (southernmost Patagonia, Demouchy et al. 2006) along [100] and [001] axes, and the results of 3D anisotropic model for diffusion of hydrogen. The size of the sample is 2.3 × 1.7 × 1.6 mm. The initial and final concentrations are, respectively, 312 and 46 ppm wt H_2O. The calculations have been conducted for different sets of diffusion coefficients (D_x', D_y', D_z') modified from PV diffusion coefficients at 1245 °C (D_x, D_y, D_z; Demouchy and Mackwell 2006, *grey* profiles in each *panel*) see text for details and discussion. In **a** only D_x' is increased. In **b** D_x' and D_y' are increased in the same way, and D_z' is decreased; In **c** D_x' is increased and D_y' and D_z' are decreased in the same way. The numerical values used and the dehydration duration required to reach the final concentration observed in the natural specimen are indicated on each plot

axes is achieved when $D_z'/D_z = 0.04$ (Fig. 7b), i.e., when D_x' and D_y' are about 15 times faster than D_z'. The change in shape of the concentration profile along [001] axis illustrated in Fig. 7b for the sets of values used even allows to provide a rough error bar on $Dz'/Dz = 0.04 \pm 0.01$. The corresponding dehydration duration from 312 to 46 ppm wt H_2O is 4.1 h and it is constant for the four sets of diffusion coefficients used in this numerical experiment.

In a third numerical experiment, we attempt to account both for the influence of pressure, which impedes diffusion, and for the PP process, which enhances diffusion along [100] axis. We hence set $D_x' = 10\ D_x$ to account for faster diffusion along [100] axis while D_y and D_z are reduced in the same way, ($D_y'/D_y = D_z'/D_z$) to account for a potential decrease of diffusivity with increased pressure (pressure effect). The resulting concentration profiles are shown in Fig. 7c for three different ratio $D_y'/D_y = D_z'/D_z$. A good fit to concentration profiles along both [100] and [001] axes is obtained when $D_y'/D_y = D_z'/D_z = 0.015 \pm 0.005$. The error bar is again a rough estimate, provided within the assumption we made, and deduced from the changes in shape of the concentration profile along [001] axis. The corresponding duration of dehydration from 312 to 46 ppm wt H_2O is 10.6 h. If 70 km is taken as origin depth for the xenoliths (D'Orazio et al. 2000; Stern et al. 1989), it yields a 1.8 ms^{-1} as ascending rate. We use the shape of the profiles to tune the relative values of diffusion coefficients, which could be characteristic of alternative possible diffusion processes. Moreover, it demonstrates that a detailed measurement of the concentration profile across samples is a real necessity since the shape of the profiles is very sensitive to the relative values of the diffusion coefficients.

Considering that olivine and pyroxene do share the same water fugacity, one can calculate the concentration in olivine using the respective solubility equations of olivine and orthopyroxene from Keppler and Bolfan-Casanova (2006). However, the solubility equations were inferred from a chemically simplified system that may lead to an overestimation of the initial concentration. We also neglect, for example, the Al dependence of hydrogen solubility of hydrogen (Stalder 2004; Mierdel et al. 2007). We have hence performed a series of calculations starting from only

150 ppm wt H_2O instead of 312 ppm wt H_2O. The resulting concentration profiles are very similar and largely within the error bars of the measurements. However, the durations of dehydration at 1245 °C are logically reduced from 4.1 to 2.8 h and from 10.6 to 3.6 h for the cases described in Fig. 7b, c, respectively. As expected, it demonstrates the limitation of the results of the models when applied to natural samples due to the uncertainty on the initial hydrogen concentration.

Since the diffusion efficiency decreases as the temperature decreases, we have investigated the influence of temperature on dehydration. Accounting for temperature dependence of diffusion coefficients requires modeling dehydration for a given duration associated with a temperature drop. We assume a linear decrease of temperature with time, from the initial (1245 °C, temperature of the mantle source at depth) to the final temperature (at the surface where the sample is quenched rapidly and diffusion stops). The diffusion coefficients are adjusted at each time step of the calculation according to the variations of diffusion coefficients with temperature given by Demouchy and Mackwell (2006) for the PV process. This can be performed since we have chosen an explicit scheme to solve the problem as explained earlier. We have performed a large series of numerical experiments corresponding to more than 150 combinations of dehydration durations and temperature drops for dehydration of olivine samples (2.3 × 1.7 × 1.6 mm as Pali-aike specimen, the initial concentration is set to 312 ppm wt H_2O) according to PV process. The results are shown in Fig. S2. It hence takes about 2.9 h to dehydrate a sample (same size as Pali-aike samples, as described above) from 312 to 46 ppm wt H_2O at a constant temperature of 1245 °C. It takes 5.4 h when a temperature drop of 100 °C is taken into account (see Kavanagh and Sparks (2009) for example of basalt cooling rates), meaning, that a temperature decrease of 100 °C in the arising magma column yields only a factor 2 on the corresponding dehydration duration.

We show that in order to fit the concentration profiles measured on Pali-aike olivines, diffusion has to be anisotropic with [100] axis being the fastest axis of diffusion and [001] axis the slowest. Diffusion along [010] axis cannot be constrained since there are no measures available. We favor the hypothesis combining the influence of pressure, reducing all diffusion coefficients along the three principal axes, and PP process effect strongly enhancing diffusion along [100] axis due to interstitial and metallic site exchange (interactions of the two processes). Our analysis shows that a good quality of measures (i.e., more than 15 points per profile, from an crystallographically oriented crystal of known size) is a strong constraint for determining empirically the relative values of diffusion coefficients along the three axes. However, the duration and hence the ascent rate are directly related to the absolute value of diffusion coefficient, which cannot be constrained by the fit of the diffusion profiles in natural specimens. Finally, experimental studies need to be conducted to confirm our hypothesis and to determine diffusion coefficients relevant to dehydration at high pressure (>1 GPa) and high temperature (800–1300 °C) with controlled geometry of the sample. In addition to temperature and pressure dependence, concentration dependence needs also to be investigated, especially close to solubility concentration for olivine and other NAMs.

Conclusion

We have shown that since diffusion of hydrogen in olivine crystal is strongly anisotropic, 3D anisotropic models are required to accurately predict the concentration profiles. The 1D plane sheet approximation is only valid for the fast axis, when the value of the diffusion coefficient along the fast axis is at least 10 times the value of the diffusion coefficients along slower axes. The concentration profiles measured for Pali-aike samples are characteristic of dehydration. However, they are neither consistent with PP process, which is too fast, nor with PV process, since a fast [001] axis is not observed. PP and PV processes can be treated as independent process for hydration. Nevertheless, we propose that the two processes may interact at atomic level when an olivine crystal is dehydrating. We have succeeded in fitting the measured Pali-aike diffusion profiles, with assuming a fast [100] axis and a [001] axis, which is 15–40 times slower than the [100] axis. The latter uncertainty comes from the fact that the diffusion profile along [010] axis could not be measured and hence could not be used to further constrain the value of the corresponding diffusion coefficient. Our results show that the shape of diffusion profiles allows to constrain relative values of diffusion coefficients at the condition to have enough measurements from natural samples. In all cases, new experimental studies have to be conducted to further determine diffusion coefficients relevant for dehydration at high pressure and temperature. The concentration profiles of hydrogen measured in mantle-derived olivine could then be used to fine-tune the dehydration time and hence the ascent rates of mantle xenoliths.

Acknowledgements We thank David Mainprice for fruitful discussions. We are also grateful to Henry Skogby and two anonymous referees whose suggestions and comments helped to improve the paper.

References

Albarède F (2009) Volatile accretion history of the terrestrial planets and dynamic implications. Nature 461(7268):1227–1233. doi:10.1038/nature08477

Bell DR, Rossman GR (1992) Water in Earth's mantle: the role of nominally anhydrous minerals. Science 255(5050):1391–1397. doi:10.1126/science.255.5050.1391

Bell DR, Rossman GR, Maldener J, Endisch D, Rauch F (2003) Hydroxide in olivine: a quantitative determination of the absolute amount and calibration of the IR spectrum. J Geophys Res. doi:10.1029/2001JB000679

Beran A, Putnis A (1983) A model of the OH positions in olivine, derived from infrared-spectroscopic investigations. Phys Chem Miner 9(2):57–60. doi:10.1007/BF00308148

Bercovici D, Karato S-I (2003) Whole-mantle convection and the transition-zone water filter. Nature 425(6953):39–44. doi:10.1038/nature01918

Berry AJ, O'Neill HSC, Hermann J, Scott DR (2007a) The infrared signature of water associated with trivalent cations in olivine. Earth Planet Sci Lett 261(1–2):134–142. doi:10.1016/j.epsl.2007.06.021

Berry A, Walker A, Hermann J, O'Neill H, Foran G, Gale J (2007b) Titanium substitution mechanisms in forsterite. Chem Geol 242(1–2):176–186. doi:10.1016/j.chemgeo.2007.03.010

Bolfan-Casanova N (2005) Water in the Earth's mantle. Mineral Mag 69(3):229–258. doi:10.1180/0026461056930248

Brodholt JP, Refson K (2000) An ab initio study of hydrogen in forsterite and a possible mechanism for hydrolytic weakening. J Geophys Res 105(B8):18977. doi:10.1029/2000JB900057

Costa F, Dungan M (2005) Short time scales of magmatic assimilation from diffusion modeling of multiple elements in olivine. Geol 33(10):837–840. doi:10.1130/G21675.1

Costa F, Dohmen R, Chakraborty S (2008) Time scales magmatic processes from modelling the zoning patterns of crystals. Rev Miner Geochim 69:545–594. doi:10.2138/rmg.2008.69.14

Crank H (1975) Mathematics of diffusion, 2nd edn. Clarendon Press, Oxford

D'Orazio M, Agostini S, Mazzarini F, Innocenti F, Manetti P, Haller MJ, Lahsen A (2000) The Pali aike volcanic field, patagonia: slab-window magmatism near the tip of South America. Tectonophysics 321(4):407–427. doi:10.1016/S0040-1951(00)00082-2

Deer WA, Howie RA, Zussman J (1997) Rock-forming minerals, orthosilicates, vol 1a. The geological society, London 696

Demouchy S, Mackwell S (2003) Water diffusion in synthetic iron-free forsterite. Phys Chem Miner 30(8):486–494. doi:10.1007/s00269-003-0342-2

Demouchy Sylvie, Mackwell S (2006) Mechanisms of hydrogen incorporation and diffusion in iron-bearing olivine. Phys Chem Miner 33(5):347–355. doi:10.1007/s00269-006-0081-2

Demouchy S, Jacobsen SD, Gaillard F, Stern CR (2006) Rapid magma ascent recorded by water diffusion profiles in mantle olivine. Geology 34(6):429–432. doi:10.1130/G22386.1

Demouchy Sylvie, Tommasi A, Barou F, Mainprice D, Cordier P (2012) Deformation of olivine in torsion under hydrous conditions. Phys Earth Planet Int 202–203:56–70. doi:10.1016/j.pepi.2012.05.001

Denis CMM, Demouchy S, Shaw CSJ (2013) Evidence of dehydration in peridotites from eifel volcanic field and estimates of the rate of magma ascent. J Volcanol Geotherm Res 258:85–99. doi:10.1016/j.jvolgeores.2013.04.010

Dixon JE, Clague DA (2001) Volatiles in basaltic glasses from Loihi Seamount, Hawaii: evidence for a relatively dry plume component. J Petrol 42(3):627–654

Férot A, Bolfan-Casanova N (2012) Water storage capacity in olivine and pyroxene to 14GPa: implications for the water content of the Earth's upper mantle and nature of seismic discontinuities. Earth Planet Sci Lett 349–350:218–230. doi:10.1016/j.epsl.2012.06.022

Gaetani GA, Grove TL (1998) The influence of water on melting of mantle peridotite. Contrib Miner Petrol 131(4):323–346. doi:10.1007/s004100050396

Gaillard F, Schmidt B, Mackwell S, Mccammon C (2003) Rate of hydrogen–iron redox exchange in silicate melts and glasses geochim. Cosmochim Acta 67(13):2427–2441. doi:10.1016/S0016-7037(00)01407-2

Giberti G, Wilson L (1990) The influence of geometry on the ascent of magma in open fissures. Bull Volcanol 52:515–521

Girona T, Costa F (2013) DIPRA: a user-friendly program to model multi-element diffusion in olivine with applications to timescales of magmatic processes. Geochem Geophys Geosyst 14(2):422–431. doi:10.1029/2012GC004427

Hirschmann MM, Aubaud C, Withers AC (2005) Storage capacity of H_2O in nominally anhydrous minerals in the upper mantle. Earth Planet Sci Lett 236(1–2):167–181. doi:10.1016/j.epsl.2005.04.022

Ihinger PD, Hervig RL, Mcmillan P (1994) Analytical methods for volatiles in glasses. In: Carroll MR, Holloway JR (eds) Volatiles in magmas. Mineralogical Soc America, Washington DC, pp 67–121

Ingrin J, Skogby H (2000) Hydrogen in nominally anhydrous upper-mantle minerals: concentration levels and implications. Eur J Miner 12(3):543–570

Ingrin J, Liu J, Depecker C, Kohn SC, Balan E, Grant KJ (2013) Low-temperature evolution of OH bands in synthetic forsterite, implication for the nature of H defects at high pressure. Phys Chem Miner 40(6):499–510. doi:10.1007/s00269-013-0587-3

Jacobsen SD, Smyth JR, Spetzler H, Holl CM, Frost DJ (2004) Sound velocities and elastic constants of iron-bearing hydrous ringwoodite. Phys Earth Planet Int 143–144:47–56. doi:10.1016/j.pepi.2003.07.019

Karato S (1990) The role of hydrogen in the electrical conductivity of the upper mantle. Nature 347(6290):272–273. doi:10.1038/347272a0

Karki BB, Verma A (2009) Ab initio investigations of point defects and ionic diffusion in bulk and grain boundary of silicate and oxide minerals. Geochim Cosmochim Acta 73:A623

Kavanagh JL, Sparks RSJ (2009) Temperature changes in ascending kimberlite magma. Earth Planet Sci Lett 286:404–413

Keppler H, Bolfan-Casanova N (2006) Thermodynamics of water solubility and partitioning. Rev Mineral Geochem 62:193–230

Kohlstedt DL, Mackwell SJ (1998) Diffusion of hydrogen and intrinsic point defects in olivine. Zeitschrift Fur Physikalische Chemie 207:147–162

Kohlstedt DL, Keppler H, Rubie DC (1996) Solubility of water in the α, β and γ phases of (Mg, Fe) 2 SiO_4. Contrib Miner Petrol 123(4):345–357. doi:10.1007/s004100050161

Le Voyer M, Asimow PD, Mosenfelder JL, Guan Y, Wallace P, Schiano P, Stolper EM, Eiler JM (2014) Zonation of H_2O and F concentrations around melt Inclusions in olivines. J Petrol 55(4):685–707. doi:10.1093/petrology/egu003

Mackwell Stephen J, Kohlstedt DL (1990) Diffusion of hydrogen in olivine: implications for water in the mantle. J Geophys Res 95(B4):5079. doi:10.1029/JB095iB04p05079

Mackwell SJ, Kohlstedt DL, Paterson MS (1985) The role of water in the deformation of olivine single crystals. J Geophys Res 90(B13):11319. doi:10.1029/JB090iB13p11319

Marty B (2012) The origins and concentrations of water, carbon, nitrogen and noble gases on Earth. Earth Planet Sci Lett 313–314:56–66. doi:10.1016/j.epsl.2011.10.040

McMillan P (1994) Water solubility and speciation models. In: Carroll MR, Holloway JR (eds) Volatiles in magmas. Mineralogical Soc America, Washington DC, pp 131–156

Mehrer H (2007) Diffusion in solids, fundamentals, methods, materials, diffusion-controlled processes. Springer, Berlin Heidelberg

Mei S, Kohlstedt DL (2000) Influence of water on plastic deformation of olivine aggregates: 1. Diffusion creep regime. J Geophys Res 105(B9):21457. doi:10.1029/2000JB900179

Mierdel K, Keppler H, Smyth JR, Langenhorst F (2007) Water solubility in aluminous orthopyroxene and the origin of Earth's asthenosphere. Science 315(5810):364–368. doi:10.1126/science.1135422

Nakamura A, Schmalzried H (1983) On the nonstoichiometry and point defects of olivine. Phys Chem Miner 10:27–37

O'Neill HS (1991) The origin of the moon and the early history of the earth—a chemical model. Part 1: the moon. Geochim Cosmochim Acta 55(4):1135–1157. doi:10.1016/0016-7037(91)90168-5

Padrón-Navarta JA, Hermann J, O'Neill HS (2014) Site-specific hydrogen rates in forsterite. Earth Planet Sci Lett 392:100–112. doi:10.1016/j.epsl.2014.01.055

Paterson MS (1982) The determination of hydroxyl by infrared-absorption in quartz, silicate-glasses and similar materials. Bull Miner 105:20–29

Peslier AH, Luhr JL (2006) Hydrogen loss from olivines in mantle xenoliths from Simcoe (USA) and Mexico: mafic alkalic magma ascent rates and water budget of the sub-continental lithosphere. Earth Planet Sci Lett 242(3–4):302–319. doi:10.1016/j.epsl.2005.12.019

Stalder R (2004) Influence of Fe, Cr and Al on hydrogen incorporation in orthopyroxene. Eur J Miner 16:703–711

Stern CR, Skewes MA, Saul S, Futa K (1989) Garnet peridotite xenoliths from the Pali-Aike alkali basalts of southernmost South America. In: Kimberlites and related rocks-their mantle and crustal setting, vol 2. Geological Society of Australia Special Publication 14, pp 735–744

Walker AM, Wright K, Slater B (2003) A computational study of oxygen diffusion in olivine. Phys Chem Miner 30(9):536–545. doi:10.1007/s00269-003-0358-7

Wood BJ (1995) The Effect of H_2O on the 410-kilometer seismic discontinuity. Science 268(5207):74–76. doi:10.1126/science.268.5207.74

Yang XZ, Keppler H (2011) In-situ infrared spectra of OH in olivine to 1100 C. Am Miner 96(2–3):451–454. doi:10.2138/am.2011.3717

Yoshino T, Matsuzaki T, Shatskiy A, Katsura T (2009) The effect of water on the electrical conductivity of olivine aggregates and its implications for the electrical structure of the upper mantle. Earth Planet Sci Lett 288(1–2):291–300. doi:10.1016/j.epsl.2009.09.032

Zhao Y-H, Ginsberg SB, Kohlstedt DL (2004) Solubility of hydrogen in olivine: dependence on temperature and iron content. Contrib Miner Petrol 147(2):155–161. doi:10.1007/s00410-003-0524-4